



ONERA/CEA Joint Research Effort on Hypersonic Separated Flows Transition: An Experimental and Computational Analysis

Clément Caillaud. Mathieu Lugrin. Sébastien Esquieu3

Abstract

This study investigates the transition to turbulence for a Cone-Cylinder-Flare (CCF) geometry in the hypersonic regime at Mach 7. Experimental and numerical analyses were conducted in a joint collaboration between CEA and ONERA in order to probe flow dynamics across a wide range of Reynolds numbers. High-frequency wall-pressure and Schlieren measurements were used to identify key instabilities, including first- and second-mode waves, and their non-linear interactions. Resolvent analysis and global stability theory were employed to characterize the dominant mechanisms driving transition. The results highlight the role of Reynolds number and flow topology in determining transition scenarios, providing insights into hypersonic boundary layer instabilities and their implications for aerodynamic design.

Keywords: hypersonic, transition, experiments, simulation

Nomenclature

Latin

M – Mach number

Re - Reynolds number

f – Frequency (Hz)

L – Length (m)

t - time (s)

m – Azimuthal wavenumber T – Temperature (K)

Greek

 δ – Boundary layer height (m)

 ρ – Density (kgm.m⁻³)

 μ – Resolvent gain

 σ – SPOD energy gain

Superscripts

* - Complex conjugate

Subscripts

opt - Optimal

e - Boundary layer edge quantities

w - Wall quantities

E - Compressible energy norm

 ∞ – Computed from the freestream values

1st - First-mode related quantity 2nd - Second-mode related quantity

1. Introduction

Understanding transition to turbulence in hypersonic flows remains a critical challenge due to the complex interplay between boundary layer instabilities, shockwave/boundary layer interactions (SBLI), and mean flow effects. This study focuses on a Cone-Cylinder-Flare (CCF) geometry. Such a geometry is particularly relevant for hypersonic reentry vehicles, as it contains the main flow features experienced by reentry vehicles during flight. The cone section simulates the nose of the vehicle and a developing boundary-layer where: lift-up, first and second Mack instabilities can grow. The cylinder starts with an expansion fan that tends to stabilize the cone instabilities. Finally, the flare mimics the aft section of a vehicle with a separated flow and a recompression region that supports most of the upstream instabilities. In this region, the separation shear layer and the recompression act as strong amplification mechanism for instabilities and numerous non-linear interactions have been observed. Therefore, understanding the transition to turbulence on this geometry is a good step towards understanding more complex transition scenarios in order to design efficient and stable hypersonic vehicles. For conciseness,

¹CEA-CESTA, 15 Avenue des Sablières, Le Barp, France, clement.caillaud@cea.fr

²DAAA ONERA, Institut Polytechnique de Paris, F-92190 Meudon

³CEA-CESTA, 15 Avenue des Sablières, Le Barp, France

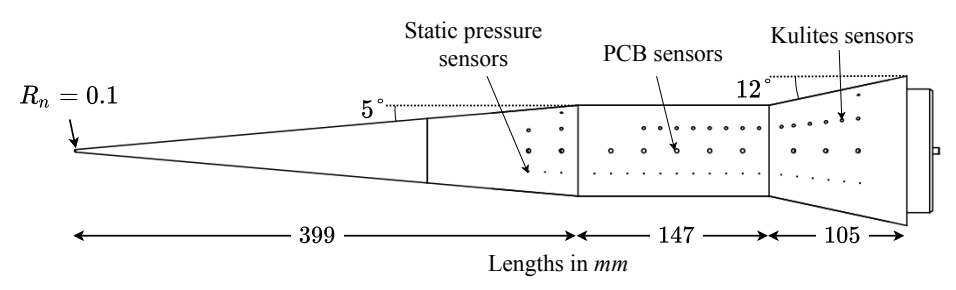


Fig 1. Schematic representation of the CCF12 model used in the experiments

Regime	Quasi-steady	-	High-frequency
Name	Static Taps	-	PCB 132B38
Number	20	-	10
Sampling Rate	100 Hz	-	3.3 MHz
Range	N/A	-	[10, 450] kHz

Table 1. Wall pressure sensors summary

only a minimal set of references are included throughout this proceeding paper. For a detailed overview of past work on the CCF12 geometry, the interested reader is invited to read the NATO AVT346 research group work [Caillaud et al., Benitez et al., 2025].

The present study extends the previous work by offering a detailed overview of these transition mechanisms by comparing experimental and numerical data. The experimental campaign, conducted in the R2Ch blow-down wind tunnel at ONERA Meudon, explored a wide range of Reynolds numbers to capture the transition from laminar to turbulent flow. High-frequency wall-pressure sensors and high-speed Schlieren imaging were used to identify the leading instabilities and their evolution. Numerical tools, including Resolvent analysis and global stability theory, complemented the experimental data to provide a comprehensive understanding of the transition mechanisms. The paper is outlined as follows, first the experimental and numerical methodologies are presented. Second, the evolution of the flow topology and boundary-layer instabilities across several Reynolds numbers is discussed. Finally, a detailed discussion is provided for two transition scenarios pertaining to small and large separated flows on the cylinder-flare region, respectively.

2. Methodology

2.1. Experimental Setup

The experiments were performed in the R2Ch wind tunnel, which operates at Mach numbers of 5, 6, and 7, with a nozzle exit diameter of 0.327m The R2Ch wind tunnel is a conventional blow-down facility that allows for the exploration of hypersonic flows under controlled conditions. The tunnel can operate at stagnation pressures ranging from 1.0 to 80 bars and stagnation temperatures from 450 to 750 K. This range of conditions enables the investigation of a wide spectrum of Reynolds numbers, making it an ideal facility for studying transition to turbulence in hypersonic flows.

The CCF model, designed by the CEA, as shown in Fig. 1, consists of a sharp nosetip, a 5° half-angle cone, a cylinder, and a 12° half-angle flare that promotes laminar boundary layer separation. The wall-pressure measurements were performed using high-frequency PCB132B38 and IC2 Mhz sensors. High-speed Schlieren imaging using a folded Z-type setup and a Phantom TMX7510 provided time-resolved density gradient measurements in two regions: the cone-cylinder junction and the cylinder-flare junction. The setup allows a fine probing of flow dynamics, including separation bubbles and instability amplification.

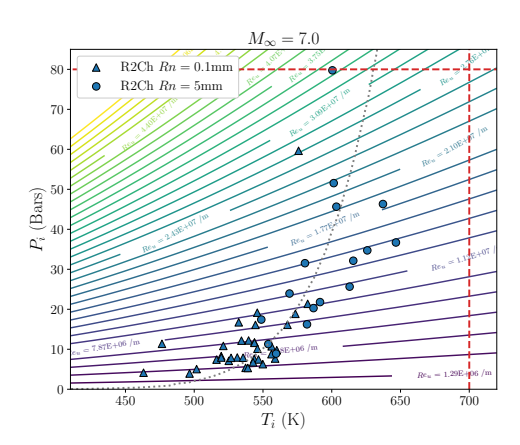


Fig 2. Summary of all the flow conditions considered in the experimental campaign.

2.2. Experimental Data Analysis

Spectral Proper Orthogonal Decomposition (SPOD) Schmidt and Colonius [2020] and Bispectral Mode Decomposition (BMD) Schmidt [2020] were used to analyze high-speed Schlieren data. SPOD, is particularly becoming a common tool to post-process high-speed Schlieren data of hypersonic instabilities in the last few years. It allows the elicitation of spatio-temporally coherent structures from the images. The BMD extends the SPOD by focusing on the non-linear interactions between these coherent structures, providing a deeper understanding of the transition process.

2.3. Numerical Base-flow and Resolvent analysis

CCF12 baseflows are computed with the BROADCAST library developed at ONERA Poulain et al. [2023]. In this study, 7th-order FE-MUSCL schemes and a Newton solver are used to obtain axisymmetric steady states q(x,t) in conservative variables, $(\rho,\rho u_x,\rho u_r,\rho u_\theta,\rho E)^T$, using cylindrical coordinates $x=(x,r,\theta)$. To perform the global stability analyses, the non-linear Navier-Stokes equations are written as the following forced non-linear dynamical system,

$$\frac{\partial}{\partial t} q(x, t) = \mathcal{N}(q(x, t)) + f_e(x, t). \tag{1}$$

With $\mathcal N$ the discrete non-linear operator of the compressible Navier-Stokes equations for a perfect gas using a Sutherland law for viscosity. The source term f_e represents the external sources of disturbances. Using the numerical baseflows, Resolvent analysis is employed to identify the leading convective instabilities at each frequency-wavenumber duet (f,m) around the laminar baseflow. This mathematical framework allows to recover the optimal responses q_{opt} , forcings f_{opt} and their associated optimal gain $\mu_{opt} = ||q_{opt}||_E/||f_{opt}||_E$ with $||.||_E$ a compressible energy norm. The baseflows were computed at $M_{\infty} = 7$, with a cold isothermal wall at $T_w = 300$ K. The inflow is imposed at the outer boundary with the measured wind-tunnel conditions for the considered Reynolds number. The outflow is taken as a zero-order extrapolation. The grids are mesh converged for all the considered disturbances wavelengths at these conditions. A detailed overview of the methodology and its application for CCF12 can be found in Refs. Poulain et al. [2023], Caillaud et al..

3. Flow Conditions Overview

3.1. Reynolds trends in flow topology

To explore the transitional dynamics of the flow around the sharp nosetip CCF12 geometry, runs were performed at a Mach number of 7 across a large range of Reynolds number. The Fig. 2 summarizes these runs by plotting each of them in the stagnation pressure & stagnation temperature space (T_i, P_i) over a map of the associated Reynolds numbers. Runs for sharp and blunt nosetip are depicted with triangle and round markers respectively. This dataset spans most of the Reynolds number and stagnation

HiSST-2025-224 Page | 3

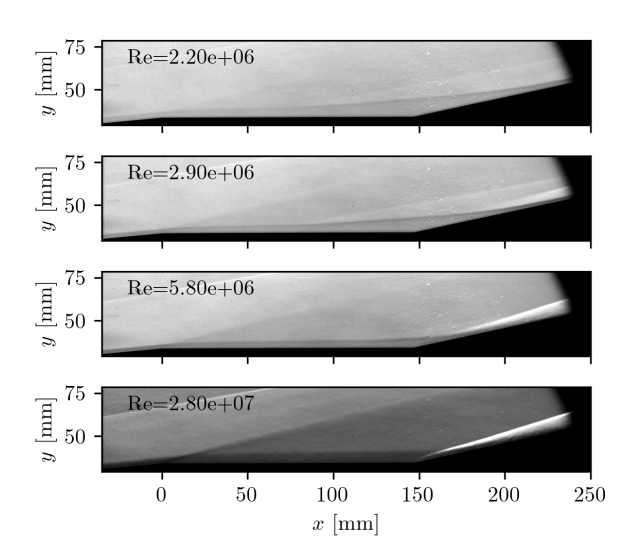


Fig 3. Mean strioscopy of the flow around CCF12 for increasing Reynolds number at $M_{\infty}=7$.

temperature range of R2Ch at both Mach numbers. The sharp nosetips ($R_n = 0.1mm$) are clustered in the lower Reynolds number range ($1.5 \times 10^6 < Re_{\infty} < 9 \times 10^6$) of R2Ch.

Previous studies have shown that, for transitional SBLI, there is a strong coupling of the separated laminar baseflow to the transition process in the separated region and thus to the incoming disturbance level in the boundary layer and the farfield. Such a coupling is observed on Fig. 3 with mean-Schlieren of the separation bubble for different Reynolds number. A clear reduction in size of the separated region can be seen as the Reynolds number increases and the separated region undergoes transition to turbulence. The reduction happens with both a downstream displacement of the separation point and an upstream displacement of the reattachment point. This shrinking of the separated region is believed to be linked to the increasing amplification rate of the instabilities with the Reynolds number. Indeed, when computing baseflows at, similar but undisturbed, conditions, it can be seen on Fig. 4 that the computed separation region continuously grows as the Reynolds number increases. The next sections explore the nature of the instabilities responsible for the shrinking of the separated region around the CCF12 geometry.

3.2. Reynolds trends in unsteady measurements

In what follows, the disturbances amplification are discussed. The optimal gain maps from a global Resolvent analysis around the object (Fig. 4) are compared to Reynolds trends in the PSD spectra from the high-speed wall-pressure sensors for the three main regions of the object: cone, cylinder & flare (Fig. 5). This overview of the most amplified instabilities serves as the basis for the specific transition scenarios discussed in the next sections. The main instabilities of this configuration, such as the first-and second-mode are directly retrieved by the optimal gain maps in Figs. 4a & 4b. For the selected Reynolds numbers of $Re_{\infty}=3.82\times10^6$ and $Re_{\infty}=6.02\times10^6$, the first-mode is visible as moderately oblique waves having a peak of gain for $f_{1st}\in[20,110]$ kHz with azimuthal wavenumbers $m\in[10,25]$. The second mode is visible as a strong gain peak for mostly planar waves $m\in[0,10]$ and frequencies $f_{2nd}\in[100,250]$ kHz. Finally, a strong amplification of steady to low frequencies and highly oblique waves is visible on the left side of the gain maps for $m\in[25,100]$, this gain peak corresponds to low frequency streamwise streaks having their highest amplification for f=0kHz. Considering these two gain maps it should also be observed that the most efficient linear instability mechanism switches between the streamwise streaks and the second-mode as the Reynolds goes from $Re_{\infty}=3.82\times10^6$ to $Re_{\infty}=6.06\times10^6$.

Reverting to the experimental data and the Fig. 5 showing the PCB sensors along the object. The second mode is visible in Fig. 5a with well-marked peaks visible between $115 \mathrm{kHz}$ and $190 \mathrm{kHz}$. The first-mode

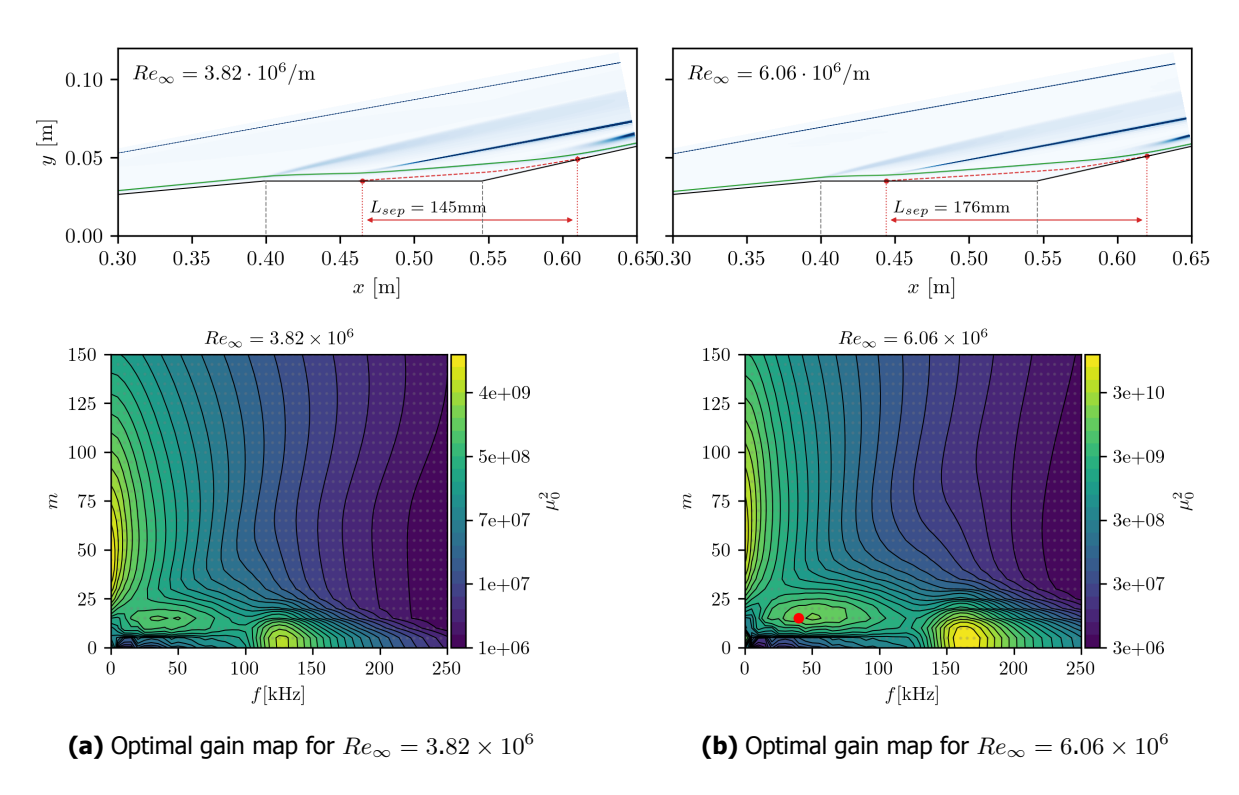


Fig 4. Overview of the baseflow and associated Resolvent optimal gain maps the Reynolds number increases. For the baseflows, boundary-layer height (—), recirculation bubble with separation and reattachment points (--)

signature is highlighted on the cylinder spectra with peaks in the range of 25kHz to 40kHz. On the flare section, the spectra are rapidly showing turbulent signature with a broadband energy content.

It is noteworthy that the cylinder pressure spectra depict a more intricate pressure signature than the cone and the flare. In addition to the two signatures of the first- and second-modes, multiple pressure peaks are visible at intermediate frequencies, these peaks appear and vanish depending on the Reynolds number. This suggests that these dynamics are related in the transitional process to specific bubble flow topologies, i.e. separation bubble lengths. This assumption is verified in more details in the following sections.

Finally, it is visible from Fig. 5 that above a Reynolds number of $Re_\infty \geq 4.77 \times 10^6$ the first-mode is not observed any more on the cylinder and the second mode is strongly amplified on the cone. Added to the remarked additional peaks, these spectrum trends in Reynolds number suggest a route to turbulence that switches from a cylinder-transition scenario for large separation at lower Reynolds number to a cone-transition scenario route for small separation at higher Reynolds number. Such a trend share similarities with reentry trajectories where the transition is often seen to move upstream along the vehicles' geometry as the Reynolds number increases. The next two sections put focus on these two distinct scenarios for which transition to turbulence is observed on the model.

4. Cone dominated transition

The regime where transition is driven by the amplification and interactions of second-mode waves is discussed by considering a case at $Re_{\infty}=6.02\times10^6$, $M_{\infty}=7.0$ and $T_i=566.1$ K. This route to turbulence will be discussed by comparing measurements obtained with PCB wall-pressure sensors, time-resolved high-speed Schlieren imagery and Resolvent analysis.

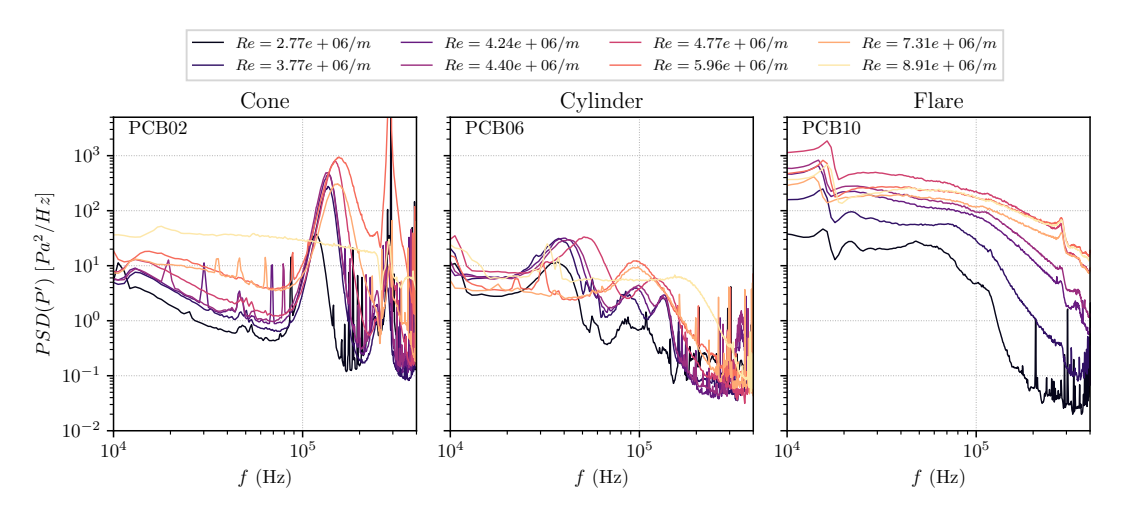


Fig 5. Comparing runs on selected PCBs at Mach= 7.0 - PCB positions need to be given

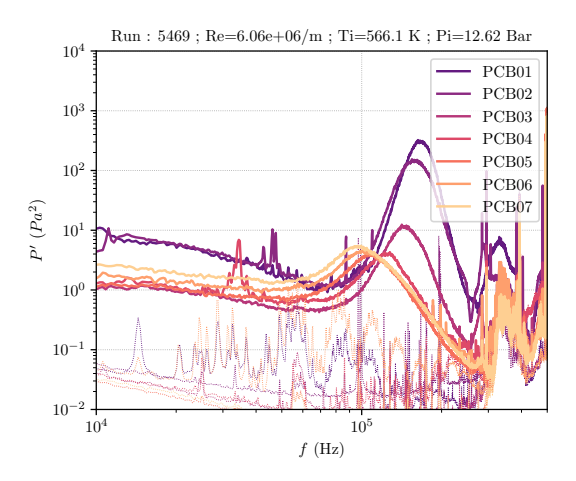


Fig 6. PCB wall pressure spectrum evolution along the geometry for $Re_{\infty} = 6.02 \times 10^6$

4.1. Wall-measurements at $Re_{\infty} = 6.06 \times 10^6$

An overview of the wall-pressure frequency spectra along the cone for these conditions is shown in Fig. 6 for the cone and cylinder sensors. All cone and cylinder spectra exhibit at least one large peak in the range $f \in [90,200]$ kHz, typical of boundary layer instabilities. On the flare, shown in Fig. 5 for this condition, a broadband spectrum, typical of the turbulence regime, is visible for $f \le 2 \times 10^5$ Hz and suggests that the flow has undergone a quick transition on the flare. The amplified peaks visible on the cone spectra in Fig. 6 are identified from the Resolvent analysis performed in Fig. 4b as being second mode waves. The evolution of the non-linearly saturating second-mode waves is further detailed in the next sections.

4.2. Optical measurements

The discussion on the peaks observed in the PCB's PSD in Fig. 6 is completed by a SPOD of the Schlieren data gathered on the cone. A frame extending from the end of the cone to the beginning of the cylinder $-22 \le x \le 33$ mm is considered. The energy content visible in the Schlieren for this region is highlighted in Fig. 7a with the SPOD energy spectrum based on light level.

Two peaks with a substantial separation are clearly visible in the SPOD energy spectrum at $f_1=175 \rm kHz$ and $f_2=350 \rm kHz$. The frequency f_1 directly matches the peak frequency observed on the cone in Fig. 6 indicating the presence of the second-mode in this region. The second peak displays an increased energy

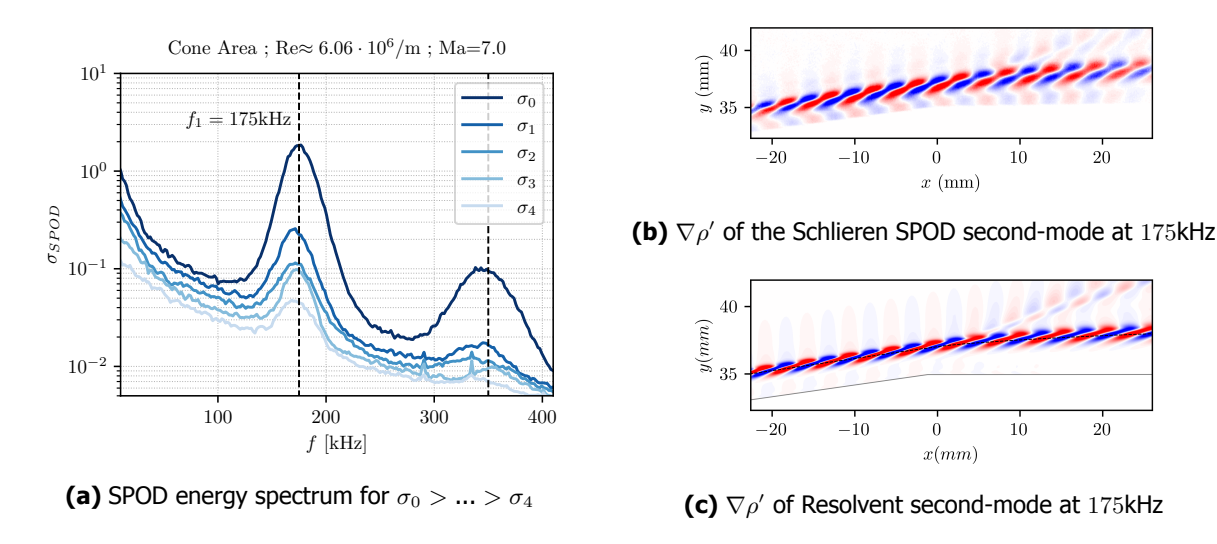


Fig 7. SPOD and Resolvent results for the cone dataset at $Re_{\infty} = 6.02 \times 10^6$

levels and is matching a triad relation $f_1 + f_1 = 2f_1$ leading to a super-harmonic, which correlates well with the non-linear broadening of the PSD peaks observed for downstream PCB sensors (Fig. 6).

Focusing on the leading SPOD mode at $f_1=175 {\rm kHz}$ shown in Fig. 7b, the second-mode is visible as a coherent structure with a short streamwise periodicity, localised along the critical-layer and close to the wall. This SPOD mode organization closely matches the resolved second mode shown in Fig. 7c, with an unprecedented level of similarity between an experimentally and numerically observed hypersonic instability. The differences reside in the organization of the most energetic regions; such discrepancies are attributed to the distortion imposed by the parallel light integration path of the Schlieren through the axisymmetric flow. Nevertheless, both the Resolvent optimal response and SPOD modes exhibit similar shapes, with a visible wall signature and energetic content being radiated outward by the expansion wave region. Such results will help future DNS studies of such transition scenarios.

4.3. Discussion on the first non-linear stages

The SPOD energy spectrum and the PCB measurements revealed a possible non-linear interaction of the second mode with the presence of multiple frequency peaks at the end of the cone region. The possible three-wave interactions are further investigated by using the bicoherence estimator,

$$S_{qqq}(f_i, f_j) = \lim_{t \to \infty} \frac{1}{t} E\left[\hat{q}^*(f_i)\hat{q}^*(f_j)\hat{q}(f_{i+j})\right], \tag{2}$$

for the measurements of IC2-02 and the complex bispectrum of the BMD, for the high-speed Schlieren dataset in the same field of view as the SPOD. Bicoherence looks for phase correlations in a signal between three waves. Using this method, triad interactions of waves in a signal, under the form of $f_1 \pm f_2 = f_3$ show as a phase correlation peak in a bispectral map spanned by (f_1, f_2) . Results from the bicoherence and BMD estimators are shown in Figs. 8a & 8b, respectively.

In both figures, peaks of phase-correlations between signals at frequencies respecting a triad-interaction are visible. Specifically, in the IC2-02 bicoherence map which offers the greatest frequency range, a rich set of triad-interactions is clearly visible as spots of phase correlations for increased multiples of the second-mode peak frequencies. As the Bicoherence estimator of Eq. 2 do not allow to obtain a causal directivity in the triad-interactions, both subtractive and additive three-waves relations have to be considered. The prevalence of one over the other is obtained through a context on the flow dynamics. Namely, the presence of a second and third super-harmonic on the IC2-02 frequency spectrum highlights the existence of additive triad-interactions $f_1 + f_1 = 2f_1 \& f_1 + 2f_1 = 3f_1$. These interactions are further confirmed by considering the BMD complex bispectrum $\lambda_1(f_i, f_j)$ in Fig. 8b as it allows distinguishing

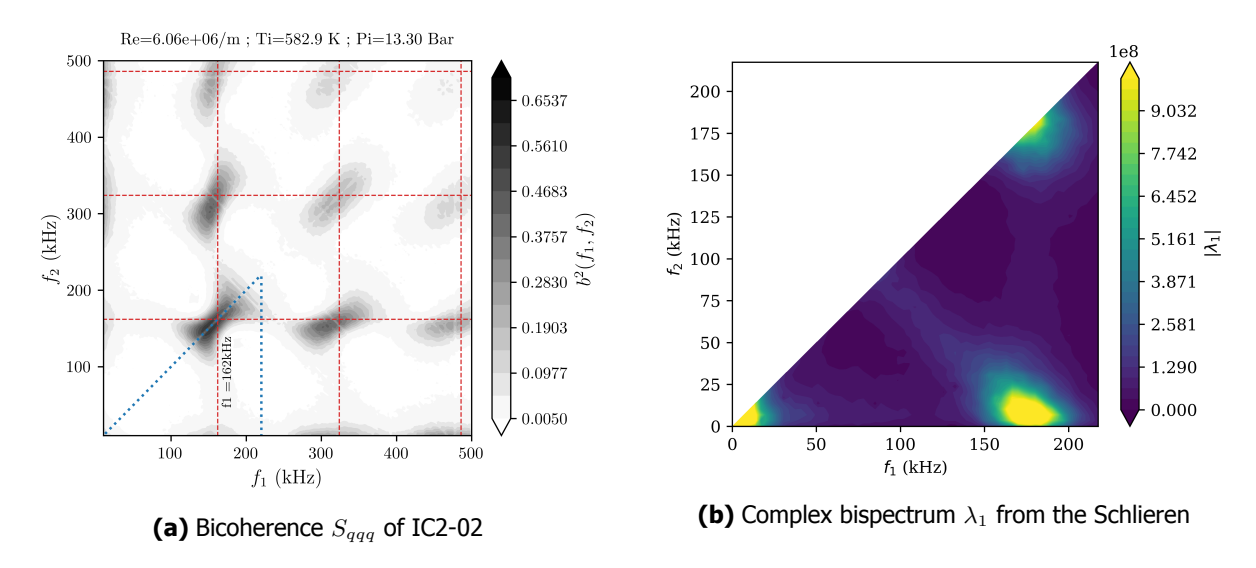


Fig 8. Bicoherence estimators from different metrologies in the cone-cylinder region. The BMD region is outlined as a blue triangle in the IC2-02 bicoherence map.

additive or subtractive interactions. Looking at its value in the positive quadrant $(0 \le f_2 \le f_1, \& f_1 \ge 0,)$ helps to observe additive energy transfers. Two leading interactions are visible at $f_1 = 175$ kHz,

$$0 + f_1 = f_1$$
 $f_1 + f_1 = 2f_1$. (3)

The former interaction indicates that the lower frequency content $0 \le f \le 20kHz$ is transferring energy to the second mode. Such interactions usually corresponds to an extraction of the energy of the baseflow from the instability. The second interaction corresponds to a first super-harmonic generation.

More details on the generation of this latter first harmonic of the second-mode are provided in Fig. 9 where the BMD is used to obtain retrieve the first-harmonic coherent structure ϕ_{i+j} (Fig. 9a) and the interaction map $\psi_{i,j}(x,y,f_i,f_j)$ in the boundary-layer (Fig. 9b) between the fundamental and first-harmonic waves of the second-mode. The first-harmonic wave displays a short wavelength structure which amplitude peaks towards the end of the cone and then displays a slow damping as the boundary layer enters the expansion region at the cone-cylinder junction. Such damping may be explained by looking at the interaction map $\psi_{i,j}(x,y,f_i,f_j)$ of Fig. 9b where the self-interaction of the second-mode at $f_{2nd}=175$ kHz clearly peaks right before the end of the cone and is then damped in the expansion region.

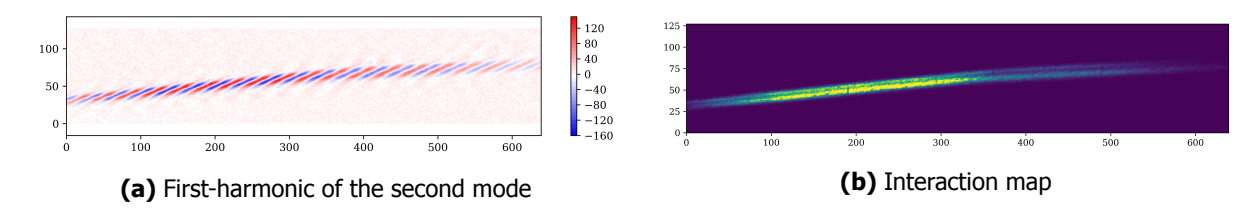


Fig 9. First-harmonic of the second mode ϕ_{i+j} and normalised interaction map $\psi_{i,j}(x,y,f_i,f_j)$ of the triad interaction $f_{2nd} + f_{2nd} = 2f_{2nd}$ from the BMD

5. Transition with a large separated region on the cylinder & flare

Owing to the flare spectra shown in Fig. 5, transition seem to first happen between $Re_{\infty}=3.77\times10^6$ & $Re_{\infty}=4.24\times10^6$. Therefore, the next section put emphasis on the route to turbulence observed in

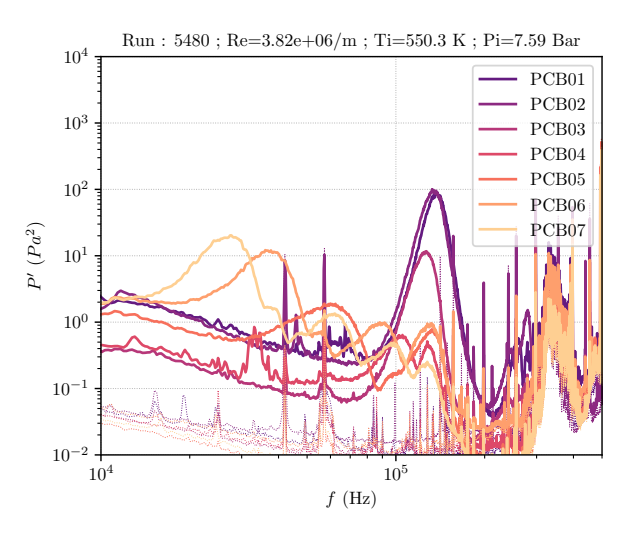


Fig 10. PCB wall pressure spectrum evolution along the geometry for $Re_{\infty}=3.82\times10^6$

that Reynolds range. A first focus is set on the PCB spectra evolution at a selected Reynolds number of $Re_{\infty}=3.82\times10^6$ in Fig. 10. The 10 PCB sensors placed along the object show a clear amplification of PSD peaks at every stations along the geometry.

5.1. Wall-measurements at $Re_{\infty}=3.82\times 10^6$

On the cone, two clear second-mode peaks can be observed around 135kHz. A slight shift toward lower frequencies and higher amplitudes is seen between PCB01 and PCB02. The shift toward lower frequencies for PCB02 is consistent with the thickening of the boundary layer and the observed growth without peak broadening suggests a linear behaviour of the second mode on the cone.

At the end of the cone, the growing second-mode passes through the cone-cylinder expansion fan. Its amplitude decreases by one order of magnitude. Such a stabilisation of the second mode is captured on the downstream sensors up to the cylinder-flare junction. Indeed, for PCB07, the amplitude of the high-frequency peak has been reduced by two order of magnitude in comparison to the cone measurements.

On the other hand, for lower frequency content, no signature is detected on the cone. However, a clear amplification of peaks below 100kHz at successive stations is visible on the cylinder in Fig. 10b from PCB04 to PCB07. This amplification is pursued along the flare as shown in Fig. 5c, with a strong wall-pressure peak for $f=20\,$ kHz. On the flare, spectral broadening is occurring as the flow is going to turbulence. A remarkable feature of this region is the presence of numerous additional peaks captured in the PSD spectra shown Fig. 5b. This observation contrasts with previous experimental observation describing only a low and a high frequency peak in the separated region, where such peaks were respectively identified as a shear-layer and a second-mode instabilities, respectively.

5.2. Optical measurements in the separated region

In Fig. 11, the wall-pressure measurements are complemented by high-speed Schlieren measurements focused on the separated region. The SPOD energy in this region displays three main peaks corresponding to instabilities at 20,45~&~125~kHz. This frequency range is consistent with the observed amplification on Resolvent gain map of Fig. 4a. Between the last two peaks at 45~&~125~kHz, a region broadband amplification is visible and matches the frequency range of the multiple peaks observed in Fig. 10 for sensors in the separated region.

The coherent structures corresponding to the three main frequency peaks of the SPOD energy spectrum are shown in Fig. 11b. These waves display high density gradient fluctuations along the shear layer with a weak radiating content within the separated region. For the last mode at $125\,\mathrm{kHz}$, the weak fluctuations in the separated region seems to match the higher acoustic oscillations discussed in the numerical study

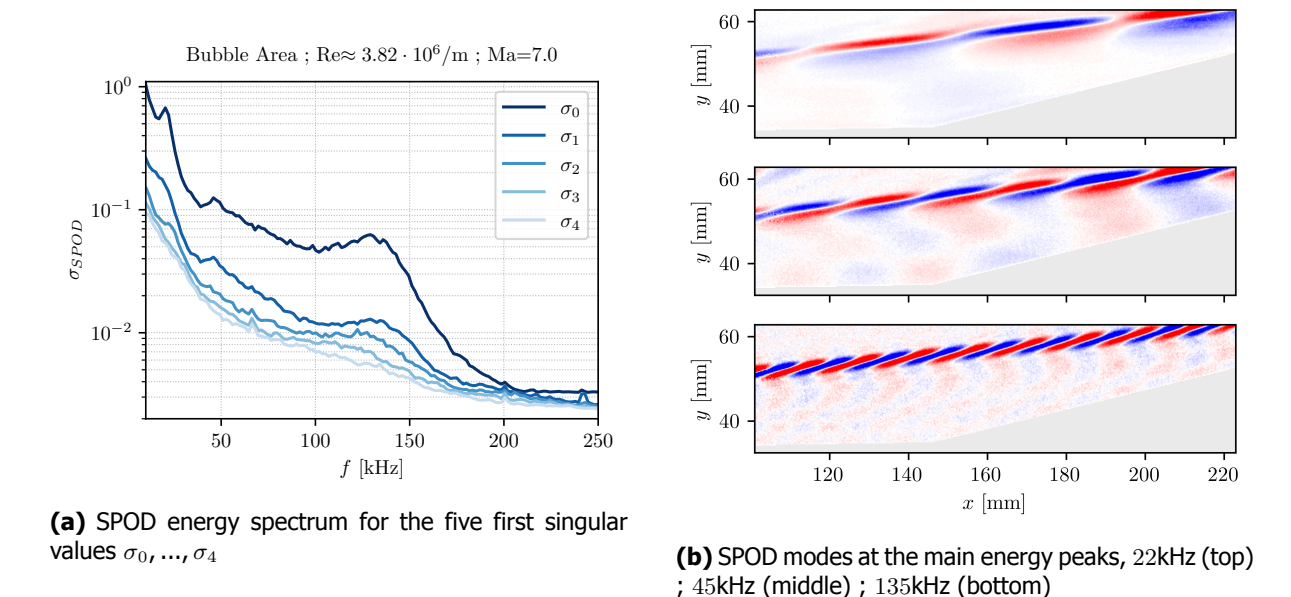


Fig 11. SPOD analysis of the separated flow region at $Re_{\infty}=3.82\times10^6$

of Ref. Caillaud et al.. The possible role of such fluctuations is discussed in the next section.

5.3. Understanding the wall pressure signature in the separated region

In order to get a more precise understanding of these multiple pressure peaks in the separated region, the Fig. 12 shows independent PSD plots of the successive PCB-sensors found from the beginning of the cone to the flare. Therefore, these sensors show the evolution of the wall pressure signature of boundary layer instabilities through the expansion fan and the separated region. To complement this experimental data and help to identify the convective mechanism underlying the peaks, pressure PSD specta reconstructed from the optimal response of the global Resolvent analysis are added over the experimental PSD plots.

Looking at the evolution of the wall-pressure spectrum from the PCB02 in Fig. 12a, the initial linear stages of the second mode growth are perfectly captured by the Resolvent. During these linear stages the second-mode exhibits an exponential growth on the cone, followed by a strong damping after the cone-cylinder expansion fan, visible on PCB03. At PCB04, the boundary layer is separated and both the Resolvent and experiments exhibit what seems to be a frequency splitting of the second mode peak. These two peaks are noted to be at $f_1=135 \rm kHz$ and $f_2=115 \rm kHz$. Looking further downstream at PCB05, the frequency splitting further increases and the peak at f_1 shows a small frequency hump in the experiment and Resolvent around $f_3=100 \rm kHz$. At PCB06, the acoustic signatures at f_1 , f_2 and f_3 are now clearly separated, underlining the presence of three distinct waves at this station. Finally, at PCB07, the mixing-layer height is close to maximum and both the experiments & Resolvent analysis display the presence of four peaks of frequencies f_1 , f_2 , f_3 & f_4 .

The increased frequency gap between f_1 and f_2 and the successive appearance of waves at f_3 & f_4 as the flow gets increasingly separated, i.e. increased mixing layer height, invites us to conjecture linear mechanisms producing a relation between the high and low frequency waves through the presence of trapped acoustic waves amplifying at resonant frequencies within the separated region. The following sections investigate two aspects of this hypothesis. The nature of the waves leading to the peaks f_1 to f_4 is verified using Resolvent and extraction of local instability profiles, not shown here for conciseness.

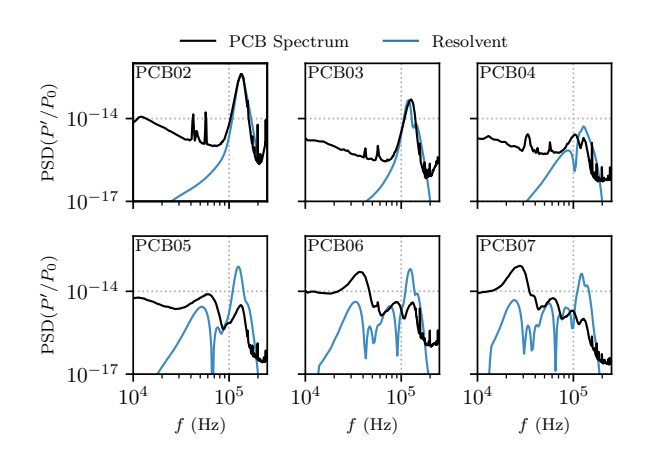


Fig 12. PCB and Resolvent wall-pressure spectrum comparison for $Re_{\infty} = 3.82 \times 10^6$

6. Conclusion

This study provides a comprehensive analysis of transition to turbulence for a Cone-Cylinder-Flare geometry in the hypersonic regime. Experimental and numerical methods were used to identify key instabilities and their non-linear interactions. The results highlight the importance of Reynolds number and flow topology in determining transition scenarios, offering valuable insights for aerodynamic design and hypersonic flow control. The key results are first, the observation and description of second-mode non-linear stages on the cone. Second, the description of the switch between transition scenarios as the Reynolds number increases and finally, the first experimental and numerical observation of trapped acoustic waves in the hypersonic separated flow. The findings of this study have important implications for the design of hypersonic vehicles. By understanding the transition mechanisms in different flow regimes, engineers can design vehicles that are more stable and efficient. This study provides a foundation for future research in this area and highlights the need for further investigation into the complex interplay between boundary layer instabilities, shockwave/boundary layer interactions, and mean flow effects in hypersonic flows.

References

- E. K. Benitez, C. Caillaud, Z. A. McDaniel, M. Lugrin, S. Esquieu, M. P. Borg, J. S. Jewell, A. Scholten, P. Paredes, F. Li, and M. M. Choudhari. Separation and transition on a cone-cylinderflare: Experimental campaigns. AIAA Journal, 63(5), 2025. doi: 10.2514/1.J064198. URL https://doi.org/10.2514/1.J064198.
- C. Caillaud, S. Esquieu, A. Scholten, P. Paredes, F. Li, M. M. Choudhari, J. Kuehl, M. Lugrin, E. K. Benitez, M. P. Borg, Z. A. McDaniel, and J. S. Jewell. Separation and Transition on a Cone-Cylinder-Flare: Computational Investigations. In AIAA SCITECH 2024 Forum. American Institute of Aeronautics and Astronautics. doi: 10.2514/6.2024-0497.
- A. Poulain, C. Content, D. Sipp, G. Rigas, and E. Garnier. BROADCAST: A high-order compressible CFD toolbox for stability and sensitivity using Algorithmic Differentiation. Computer Physics Communications, 283:108557, Feb. 2023. ISSN 0010-4655. doi: 10.1016/j.cpc.2022.108557.
- O. T. Schmidt. Bispectral mode decomposition of nonlinear flows. Nonlinear Dynamics, 102(4):2479-2501, Dec. 2020. ISSN 0924-090X, 1573-269X. doi: 10.1007/s11071-020-06037-z.
- O. T. Schmidt and T. Colonius. Guide to Spectral Proper Orthogonal Decomposition. AIAA Journal, 58 (3):1023–1033, Mar. 2020. ISSN 0001-1452, 1533-385X. doi: 10.2514/1.J058809.